A Spectral-Element Discontinuous Galerkin Lattice Boltzmann Method for Simulating Natural Convection Heat Transfer in a Horizontal Concentric Annulus

Saumil Sudhir Patel[a], Misun Min[b], Kalu Chibueze Uga[a], Taehun Lee[a,*]

[a]*Department of Mechanical Engineering, City College of City University of New York, New York, NY 10031, USA*
[b]*Mathematics and Computer Science Division, Argonne National Laboratory, Argonne, IL 60439, USA*

Abstract

We present a spectral-element discontinuous Galerkin lattice Boltzmann method to solve incompressible natural convection flows based on the Bousinessq approximation. A passive-scalar thermal lattice Boltzmann model is used to resolve flows for variable Prandtl number. In our model, we solve the lattice Boltzmann equation for the velocity field and the advection-diffusion equation for the temperature field, reducing the degrees of freedom compared with the passive-scalar double-distribution model, which requires the solution of an additional set of evolution equations to resolve the temperature field. Our numerical solution is represented by the tensor product basis of the one-dimensional Legendre-Lagrange interpolation polynomials on the Gauss-Lobatto-Legendre quadrature nodes and body-conforming hexahedral elements. Within the discontinuous Galerkin framework, we impose boundary and element-interface conditions weakly through the numerical flux. A fourth-order Runge-Kutta scheme is used for time integration with simple mass matrix inversion due to fully diagonal mass matrices. We studied natural convection fluid flows in a square cavity and a horizontal concentric annulus for Rayleigh numbers in the range of Ra=10^3∼10^5. Validation of our numerical approach is conducted by comparing with finite-difference, finite-

*Corresponding Author
Email addresses: saumil.patel134@gmail.com (Saumil Sudhir Patel), mmin@mcs.anl.gov (Misun Min), uga.kalu@gmail.com (Kalu Chibueze Uga), thlee@ccny.cuny.edu (Taehun Lee)

volume, multiple-relaxation-time lattice Boltzmann, and spectral-element methods. Compared with other methods, our computational results show good agreement in temperature profiles and Nusselt numbers using relatively coarse resolutions.

Keywords: Thermal lattice Boltzmann method, Spectral-element method, Discontinuous Galerkin method, Natural convection flow

1. Introduction

Natural convection flow simulations have been an active area of research for many years. These flows are set in motion by a buoyancy force, which occurs as a result of a small density gradient and the presence of an external force such as gravity. Understanding the behavior of natural convection flows is important in nuclear reactor design, cooling of electronic equipment, and determination of heat loss from steam pipes.

In recent decades, thermal lattice Boltzmann methods (TLBMs) have emerged as reliable methods for simulating natural convection flows. TLBMs generally fall into two approaches: the multispeed approach and the passive-scalar approach. The multispeed approach is an extension of the isothermal model, where the density distribution function is solely used to describe the mass, momentum, and temperature [1, 2]. The passive-scalar approach uses additional equation(s), independent of the density distribution, to describe the temperature. When viscous heating and compression work due to pressure are negligible, as is the case in most natural convection flows, the temperature does not influence the momentum—it is advected and diffused "passively" [3].

The multispeed approach does have limitations. In particular, it suffers from severe numerical instability and restricts the Prandtl (Pr) number to a fixed quantity [1]. However, numerous models have been proposed to rectify these issues. In [4], McNamara *et al.* were able to improve the stability by implementing a Lax-Wendroff advection scheme. Using higher-order symmetric velocity lattices, Vahala *et al.* [5] showed better stability properties over lower-order symmetric lattices. Prasianakis and Karlin [6] built a model using the standard velocity lattice (D2Q9), which incorporated equilibrium expansions up to the fourth-order in velocity and correction terms to the lattice Boltzmann equation (LBE) in order to enhance stability for high Rayleigh number (Ra) flow. The correction terms also allowed their model to

investigate variable Pr. Watari and Tsutahara [7] proposed a finite-difference lattice Boltzmann method (FDLBM), which utilized a second-order upwinding difference scheme, to improve stability. And to investigate variable Pr, Soe *et al.* [8] introduced an extended collision matrix without affecting the stability.

One of the passive-scalar approaches utilizes a double-distribution model based on the multiple component LBE proposed by Shan and Chen [3]. In this approach, one component (i.e. density distribution function) represents motion of the fluid and the other (i.e. energy distribution function) describes the passive temperature field. Two independent relaxation times are utilized for each component, thus allowing for variable Pr. In [9], Shan showed that the double-distribution model enhanced numerical stability over the multi-speed approach for high Ra. He *et al.* [10] also proposed a double-distribution model where the density distribution function recovers the macroscopic mass and momentum variables while an internal energy density distribution function recovers the energy. Because the model in [10] directly solves evolution of the internal energy, a Chapman-Enskog multiscale expansion analysis shows that viscous heat dissipation and compression work are correctly recovered in the macroscopic energy equation.

Since the work of He *et al.* [10], simpler double-distribution models have been proposed in the incompressible limit. Both, Palmer *et al.* [11] and Peng *et al.* [12] neglected viscous dissipation entirely and dropped complicated spatial gradients to study Rayleigh-Bénard convection and natural convection within a square cavity. In [13], Shi *et al.* proposed a double-distribution model that incorporates only viscous heat dissipation to study thermal Couette flow. Guo *et al.* [14] proposed a double-distribution model based on the total energy, which allows for a simpler computation of viscous dissipation and compression work. Others have proposed smaller lattice velocity models for the energy distribution functions [15].

The double-distribution model has also been used on irregular or unstructured grids to handle natural convection flows. Dixit and Babu [16] employed an interpolation supplemented lattice Boltzmann method [17] on a nonuniform mesh to study natural convection in a square at high $Ra > 10^6$. Shi *et al.* [18] extended the method proposed by Guo and Zhao [19] and used FDLBM on the polar representation of the double-distribution model. Shu *et al.* [20] used a Taylor series expansion and least squares-based lattice Boltzmann method (TLLBM) to solve the double-distribution model. The TLLBM has proved useful for complex geometries [21]. Finite-volume lattice

Boltzmann methods have also been proposed and implemented on unstructured meshes [22]. Although these methods have been applied to isothermal flows, an extension to either a multispeed or double-distribution model seems feasible.

Another passive-scalar approach is to solve the macroscopic energy equation for the temperature, coupling with the isothermal LBE for solving the velocity. This approach is particularly beneficial for flows with negligible viscous dissipation, and therefore the macroscopic energy equation simplifies to an advection-diffusion equation for the temperature. This model eliminates the need to solve multiple equations, based on the Hermite expansion of the equilibrium distribution function, in the double-distribution model. In addition, flows with variable Pr number can be investigated. Lallemand and Luo [23], proposed this type of approach, solving the advection-diffusion equation for the temperature using a finite-difference method. They showed enhanced stability for simple Cartesian geometries such as a cubic box. For complex geometries, however, finite-difference stencils may not have the same symmetries as the underlying discrete velocity, and extrapolation might cause loss of local conservation.

Implementation of physically accurate hydrodynamic and thermal boundary conditions is crucial in both the multispeed and passive-scalar models. Extensive work on boundary treatment techniques has been done and we refer the reader to the following literature [24]–[30].

In this paper we present a spectral-element discontinuous Galerkin method applied to a thermal lattice Boltzmann model based on the passive-scale approach. Our numerical scheme is extended from the previously developed spectral-element discontinuous Galerkin lattice Boltzmann method (SEDG-LBM) presented in [31]. In this work, we incorporate the discrete Boltzmann equation (DBE) and lattice Boltzmann equation (LBE) with a forcing term resulting from the Bousinessq approximation [9]. This allows us to examine flows in the incompressible limit for low Mach (Ma) numbers and small density fluctuations.

We use the SEDG-LBM to solve the density distribution function for the mass and momentum conservation laws and to determine the temperature field we solve the advection-diffusion (i.e. energy) equation using an SEDG weak form approximation. We use a high-order spectral-element discontinuous Galerkin discretization based on the tensor product basis of the one-dimensional Legendre-Lagrange interpolation polynomials on the Gauss-Lobatto-Legendre grid points on body-conforming hexahedral elements. Bounce-

back boundary conditions are applied weakly through the numerical flux without the additional effort of interpolation for complex geometries as required by other lattice Boltzmann (LB) schemes [25, 26, 27].

The paper is organized as follows. In Section 2, we present the governing equations, namely, the LBE with a Bousinessq approximation and the advection-diffusion equation. In Section 3, we discuss the formulation of our numerical scheme. Section 4 demonstrates computational results and their validation for natural convection heat transfer in a square cavity and horizontal concentric annulus. We present out conclusions in Section 5.

2. Governing Equations

In this section we describe our governing equations for natural convection flows. We derive the lattice Boltzmann equation with a forcing term and the formulation for the collison and streaming steps. We also present a simplified macroscopic energy equation for incompressible natural convection flows.

2.1. Lattice Boltzmann Equation: Collision and Streaming

We write the discrete Boltzmann equation with a forcing term, where the collision term is approximated by the Bhatnagar-Gross-Krook, or single-relaxation-time, operator [32]:

$$\frac{\partial f_\alpha}{\partial t} + \mathbf{e}_\alpha \cdot \nabla f_\alpha = -\frac{f_\alpha - f_\alpha^{eq}}{\lambda} + \frac{(\mathbf{e}_\alpha - \mathbf{u}) \cdot \mathbf{G} f_\alpha^{eq}}{\rho c_s^2} \quad \text{on} \quad \Omega, \tag{1}$$

where f_α ($\alpha = 0, 1, ..., N_\alpha$) is the particle density distribution function defined in the direction of the microscopic velocity $\mathbf{e}_\alpha$, λ is the relaxation time, and N_α is the number of microscopic velocity. We consider the two-dimensional 9-velocity model (D2Q9) associated with $\mathbf{e}_\alpha = (0, 0)$ for $\alpha = 0$; $\mathbf{e}_\alpha = (\cos\theta_\alpha, \sin\theta_\alpha)$ with θ_α=$(\alpha - 1)\pi/2$ for $\alpha = 1, 2, 3, 4$; and $\mathbf{e}_\alpha = \sqrt{2}(\cos\phi_\alpha, \sin\phi_\alpha)$ with ϕ_α=$(\alpha - 5)\pi/2 + \pi/4$ for $\alpha = 5, 6, 7, 8$. The second term on the right-hand side of Eq. (1) represents the forcing term. $\mathbf{G}$ is the external body force, depending on space and time. We consider a Bousinessq approximation for $\mathbf{G}$, which will be discussed in Section 4. The equilibrium distribution function is given by

$$f_\alpha^{eq} = t_\alpha \rho \left[1 + \frac{(\mathbf{e}_\alpha \cdot \mathbf{u})}{c_s^2} + \frac{(\mathbf{e}_\alpha \cdot \mathbf{u})^2}{2c_s^4} - \frac{(\mathbf{u} \cdot \mathbf{u})}{2c_s^2} \right], \tag{2}$$

where ρ is the density, $\mathbf{u}$ is the macroscopic velocity, $t_0 = 4/9$, $t_{\alpha=1,4} = 1/9$, and $t_{\alpha=5,8} = 1/36$ are the weights, and $c_s = 1/\sqrt{3}$ is the speed of sound [33].

We obtain the LBE by discretizing Eq. (1) along characteristics over the time step δt as shown in [31].

$$f_\alpha(\mathbf{x}, t) - f_\alpha(\mathbf{x} - \mathbf{e}_\alpha \delta t, t - \delta t) = -\int_{t-\delta t}^{t} \frac{f_\alpha - f_\alpha^{eq}}{\lambda} dt' + \int_{t-\delta t}^{t} \frac{(\mathbf{e}_\alpha - \mathbf{u}) \cdot \mathbf{G} f_\alpha^{eq}}{\rho c_s^2} dt' \tag{3}$$

Applying the trapezoidal rule for the integration on the right-hand side of Eq. (3), we have the following for each term

$$-\int_{t-\delta t}^{t} \frac{f_\alpha - f_\alpha^{eq}}{\lambda} dt' \approx -\frac{f_\alpha - f_\alpha^{eq}}{2\tau}|_{(\mathbf{x}-\mathbf{e}_\alpha\delta t, t-\delta t)} - \frac{f_\alpha - f_\alpha^{eq}}{2\tau}|_{(\mathbf{x},t)} \tag{4}$$

and

$$\int_{t-\delta t}^{t} \frac{(\mathbf{e}_\alpha - \mathbf{u}) \cdot \mathbf{G} f_\alpha^{eq}}{\rho c_s^2} dt' \approx \delta t \frac{(\mathbf{e}_\alpha - \mathbf{u}) \cdot \mathbf{G} f_\alpha^{eq}}{2\rho c_s^2}|_{(\mathbf{x}-\mathbf{e}_\alpha\delta t, t-\delta t)} + \delta t \frac{(\mathbf{e}_\alpha - \mathbf{u}) \cdot \mathbf{G} f_\alpha^{eq}}{2\rho c_s^2}|_{(\mathbf{x},t)}, \tag{5}$$

where the dimensionless relaxation time is $\tau = \lambda/\delta t$ with a relation to the kinematic viscosity by $\nu = \tau c_s^2 \delta t$.

We now introduce a modified particle distribution function $\bar{f}_\alpha$ and its corresponding equilibrium distribution function $\bar{f}_\alpha^{eq}$ [32] defined as

$$\bar{f}_\alpha = f_\alpha + \frac{f_\alpha - f_\alpha^{eq}}{2\tau} - \frac{(\mathbf{e}_\alpha - \mathbf{u}) \cdot \mathbf{G} f_\alpha^{eq}}{2\rho c_s^2} \delta t \tag{6}$$

and

$$\bar{f}_\alpha^{eq} = f_\alpha^{eq} - \frac{(\mathbf{e}_\alpha - \mathbf{u}) \cdot \mathbf{G} f_\alpha^{eq}}{2\rho c_s^2} \delta t. \tag{7}$$

Substituting Eqs. (4)–(7) into Eq. (3), we have

$$\begin{aligned} \bar{f}_\alpha(\mathbf{x}, t) &= \bar{f}_\alpha(\mathbf{x} - \mathbf{e}_\alpha \delta t, t - \delta t) - \frac{1}{\tau + 1/2} \left(\bar{f}_\alpha - \bar{f}_\alpha^{eq} \right) |_{(\mathbf{x}-\mathbf{e}_\alpha\delta t, t-\delta t)} \\ &+ \delta t \frac{(\mathbf{e}_\alpha - \mathbf{u}) \cdot \mathbf{G} f_\alpha^{eq}}{\rho c_s^2}|_{(\mathbf{x}-\mathbf{e}_\alpha\delta t, t-\delta t)}. \end{aligned} \tag{8}$$

Following the similar manner as in [31], we solve Eq. (8) in two steps:

- **Collision**

$$\begin{aligned} \bar{f}^*_\alpha(\mathbf{x}, t-\delta t) &= \bar{f}_\alpha(\mathbf{x}, t-\delta t) - \frac{1}{\tau + 1/2}\left(\bar{f}_\alpha - \bar{f}^{eq}_\alpha\right)|_{(\mathbf{x}, t-\delta t)} \\ &+ \delta t \frac{(\mathbf{e}_\alpha - \mathbf{u}) \cdot \mathbf{G} f^{eq}_\alpha}{\rho c_s^2}|_{(\mathbf{x}, t-\delta t)} \end{aligned} \tag{9}$$

  which is followed by the substitution $\bar{f}_\alpha(\mathbf{x}, t-\delta t) = \bar{f}^*_\alpha(\mathbf{x}, t-\delta t)$.

- **Streaming**

$$\bar{f}_\alpha(\mathbf{x}, t) = \bar{f}_\alpha(\mathbf{x} - \mathbf{e}_\alpha \delta t, t - \delta t). \tag{10}$$

The density and momentum can be computed by taking moments as follows:

$$\rho = \sum_{\alpha=0}^{8} \bar{f}_\alpha \quad \text{and} \quad \rho\mathbf{u} = \sum_{\alpha=0}^{8} \mathbf{e}_\alpha \bar{f}_\alpha + \frac{\delta t}{2}\mathbf{G}. \tag{11}$$

The streaming step can be expressed as a solution of the pure advection equation in an Eulerian framework [34], which can be expressed as follows:

$$\frac{\partial \bar{f}_\alpha}{\partial t} + \mathbf{e}_\alpha \cdot \nabla \bar{f}_\alpha = 0. \tag{12}$$

2.2. Energy Equation: Advection-Diffusion Equation

The temperature is modeled with the macroscopic energy equation. Assuming the flow to be incompressible and compression work due to pressure to be negligible, we can simplify the energy equation to the following advection-diffusion equation:

$$\frac{\partial T}{\partial t} + \mathbf{u} \cdot \nabla T = \chi \nabla^2 T, \tag{13}$$

where $\chi = \frac{\kappa}{\rho c_p}$ is the thermal diffusivity with the specific heat at constant pressure c_p and the thermal conductivity κ.

3. Numerical Discretization

In this section, we describe our computational scheme, including a discontinuous Galerkin weak formulation, spectral element discretization, numerical flux, and time-stepping scheme.

3.1. Weak Formulation of the LB Advection Equation

We formulate a weak form of Eq. (12) defined on the computational domain $\Omega = \cup_{e=1}^{E} \Omega^e$ with nonoverlapping elements Ω^e. Choosing proper test functions ϕ_α and multiplying it to Eq. (12) and integrating by parts twice with a numerical flux term $\mathbf{F}^*_\alpha$ introduced in the similar manner as in [31], we obtain the following weak formulation:

$$\left(\frac{\partial \bar{f}_\alpha}{\partial t} + \nabla \cdot \mathbf{F}_\alpha(\bar{f}), \phi_\alpha\right)_{\Omega^e} = \left(\mathbf{n} \cdot \left[\mathbf{F}_\alpha(\bar{f}) - \mathbf{F}^*_\alpha(\bar{f})\right], \phi_\alpha\right)_{\partial\Omega^e}, \tag{14}$$

where $\mathbf{F}_\alpha(\bar{f}) = \mathbf{e}_\alpha \bar{f}_\alpha$ represents the flux vector with the microscopic velocities $\mathbf{e}_\alpha = (e_{\alpha x}, e_{\alpha y})$ and $\mathbf{n} = (n_x, n_y)$ is the unit normal vector pointing outward on the element boundary $\partial\Omega^e$.

The numerical flux $\mathbf{F}^*_\alpha(\bar{f}) = \mathbf{F}^*_\alpha(\bar{f}, \bar{f}^+)$ in Eq. (14) is a function of the local solution $\bar{f}_\alpha$ and the neighboring solution $\bar{f}^+_\alpha$ at the interfaces between neighboring elements. We choose the Lax-Friedrichs flux in [31, 35] expressed as the following:

$$\mathbf{n} \cdot (\mathbf{F}_\alpha - \mathbf{F}^*_\alpha) = \begin{cases} (\mathbf{n} \cdot \mathbf{e}_\alpha)[\bar{f}_\alpha - \bar{f}^+_\alpha] & \text{for } \mathbf{n} \cdot \mathbf{e}_\alpha < 0, \\ 0 & \text{for } \mathbf{n} \cdot \mathbf{e}_\alpha \geq 0. \end{cases} \tag{15}$$

When $\mathbf{n} \cdot \mathbf{e}_\alpha < 0$, we can write

$$\mathbf{n} \cdot (\mathbf{F}_\alpha - \mathbf{F}^*_\alpha) = (n_x e_{\alpha x} + n_y e_{\alpha y})\bar{f}_\alpha + (n^+_x e_{\alpha x} + n^+_y e_{\alpha y})\bar{f}^+_\alpha. \tag{16}$$

The proper upwinding scheme, inherent in the Lax-Friedrichs flux, allows momentum transfer at the element interface to depend only on those particles that are entering into the element.

Boundary conditions are weakly imposed through the numerical flux. The wall boundary condition, with specific details provided in [24, 31], is given as follows:

$$\bar{f}_\alpha - \bar{f}^+_\alpha = \begin{cases} \bar{f}_\alpha - \bar{f}_{\alpha^*} - 2t_\alpha \rho_0 (\mathbf{e}_\alpha \cdot \mathbf{u}_b)/c_s^2 & \text{for } \mathbf{n} \cdot \mathbf{e}_\alpha < 0 \\ 0 & \text{for } \mathbf{n} \cdot \mathbf{e}_\alpha \geq 0, \end{cases} \tag{17}$$

where $\bar{f}_{\alpha^*}$ is the particle distribution function moving in the opposite direction of $\bar{f}_\alpha$, $\mathbf{u}_b$ is the macroscopic velocity prescribed at the wall boundary, and ρ_0 is the reference density, chosen to be unity.

3.2. Weak Formulation of the Advection-Diffusion Equation

Applying the incompressible assumption and expressing Eq. (13) as a system of first-order equations [35], we have

$$\frac{\partial T}{\partial t} + \nabla\cdot(\mathbf{u}T) = \nabla\cdot\mathbf{q}, \tag{18}$$

$$\mathbf{q} = \chi\nabla T. \tag{19}$$

We define a flux vector by $\mathbf{F}(T) = \mathbf{u}T = (u_xT, u_yT)$ and introduce numerical fluxes $\mathbf{F}^*$, $\mathbf{q}^*$ and T^*. Similarily as in Eq. (14) [31], we define proper test functions $\bar{\phi}$ and $\bar{\bar{\phi}}$ and obtain a set of weak formulation for Eqs. (18)–(19) as

$$\left(\frac{\partial T}{\partial t} + \nabla\cdot(\mathbf{F}(T) - \mathbf{q}), \bar{\phi}\right)_{\Omega^e} = \left(\mathbf{n}\cdot[\mathbf{q}^* - \mathbf{q}] - \mathbf{n}\cdot[\mathbf{F}^* - \mathbf{F}], \bar{\phi}\right)_{\partial\Omega^e} \tag{20}$$

$$\left(\mathbf{q} - \chi\nabla T, \bar{\bar{\phi}}\right)_{\Omega^e} = \chi\left(\mathbf{n}\left[T^* - T\right], \bar{\bar{\phi}}\right)_{\partial\Omega^e}. \tag{21}$$

We use the Lax-Friedrich flux for $\mathbf{F}^*$ in Eq. (21), defined by

$$\mathbf{F}^*(T, T^+) = \frac{1}{2}\left[\mathbf{F}(T) + \mathbf{F}(T^+)\right] + \frac{C}{2}\left[\mathbf{n}(T - T^+)\right], \tag{22}$$

where

$$C = \max\left|\mathbf{n}\cdot\frac{\partial\mathbf{F}}{\partial T}\right| = \max\left|\mathbf{n}\mathbf{u}\right|, \tag{23}$$

and the central flux for $\mathbf{q}^*$ and T^* in Eqs. (21)–(20),

$$\mathbf{q}^* = \frac{1}{2}\left[\mathbf{q} + \mathbf{q}^+\right] \quad \text{and} \quad T^* = \frac{1}{2}\left[T + T^+\right]. \tag{24}$$

We have nonhomogeneous wall boundary conditions defined as below for the different variables [35].
(i) Nonhomogeneous wall boundary conditions for T, i.e., $T = f(t)$:

$$T^+ = -T + 2f, \quad \mathbf{q}^+ = \mathbf{q}, \quad (\mathbf{u}T)^+ = \mathbf{u}T. \tag{25}$$

(ii) Nonhomogeneous wall boundary conditions for $\mathbf{q}$, i.e., $\mathbf{q} = \mathbf{f}(t)$:

$$T^+ = T, \quad \mathbf{q}^+ = -\mathbf{q} + 2\mathbf{f}(t), \quad (\mathbf{u}T)^+ = \mathbf{u}T. \tag{26}$$

3.3. Spectral Element Discretizations

We seek a local approximate solution u^N on Ω^e expressed by the finite expansion of the basis $\psi_{ij}(\xi,\eta)$ as

$$u^N(x,y,t) = \sum_{i,j=0}^{N} (u^N)_{ij}\psi_{ij}(\xi,\eta), \tag{27}$$

where $(u^N)_{ij} = u^N(x_i, y_j, t)$ represents the approximate solution u^N on the nodal points (x_i, y_j) at time t and $\psi_{ij}(\xi,\eta) = l_i(\xi(x))l_j(\eta(y))$, or simply ψ_{ij}, is the tensor product basis of the one-dimensional Legendre-Lagrange interpolation polynomials

$$l_i(\xi) = N(N+1)^{-1}(1-\xi^2)L'_N(\xi)/(\xi-\xi_i)L_N(\xi_i) \;\text{ for }\; \xi \in [-1,1], \tag{28}$$

based on the Gauss-Lobatto-Legendre (GLL) quadrature nodes ξ_i where $L_N(\xi)$ is the Nth-order Legendre polynomial. The physcial domain $(x,y) \in \Omega^e$ is mapped to the reference domain $(\xi,\eta) \in [-1,1]^2$, through the Gordon-Hall mapping [36].

Let us denote our approximate solutions by $\bar{f}^N_\alpha$ for the density distribution functions, T^N for the temperature, and $q^N = (q^N_x, q^N_y)$ for the auxiliary function and express each component in the form of (27). Choosing $\psi_{\hat{i}\hat{j}} = l_{\hat{i}}(\xi(x))l_{\hat{j}}(\eta(y))$ with a different index set for each test function ϕ_α, $\bar{\phi}$, and $\bar{\bar{\phi}}$ and plugging the approximate solutions into the corresponding weak formulations Eqs. (14), (18), and (19), we get a set of semidiscrete schemes

$$\frac{d\mathbf{f}_\alpha}{dt} + \mathbf{M}^{-1}\mathbf{D}_1\mathbf{f}_\alpha = \mathbf{M}^{-1}\mathbf{R}_1\mathbf{f}_\alpha, \tag{29}$$

$$\frac{d\mathbf{T}}{dt} + \mathbf{M}^{-1}\mathbf{D}_2\mathbf{T} - \mathbf{M}^{-1}\mathbf{D}\mathbf{q} = \mathbf{M}^{-1}(\mathbf{R}\mathbf{q} - \mathbf{R}_2\mathbf{T}), \tag{30}$$

$$\mathbf{q}_x - \chi\mathbf{M}^{-1}\mathbf{D}_x\mathbf{T} = \chi\mathbf{M}^{-1}\mathbf{R}_x\mathbf{T}, \tag{31}$$

$$\mathbf{q}_y - \chi\mathbf{M}^{-1}\mathbf{D}_y\mathbf{T} = \chi\mathbf{M}^{-1}\mathbf{R}_y\mathbf{T}, \tag{32}$$

where the solution vectors are defined by $\mathbf{f}_\alpha = [(\bar{f}^N_\alpha)_{ij}]$, $\mathbf{T} = [T^N_{ij}]$, and $\mathbf{q} = (\mathbf{q}_x, \mathbf{q}_y)$ with $\mathbf{q}_x = [(q^N_x)_{ij}]$, and $\mathbf{q}_y = [(q^N_y)_{ij}]$ on a local element. The mass matrix is defined as

$$\mathbf{M} = (\psi_{ij}, \psi_{\hat{i}\hat{j}})_{\Omega^e} = J(\hat{M} \otimes \hat{M}), \tag{33}$$

where $\hat{M}_{\hat{i}i} = \sum_{k=0}^{N} l_{\hat{i}}(\xi_k)l_i(\xi_k)w_k$ is the one-dimensional mass matrix with the quadrature weight w_k defined on the reference domain $[-1,1]$ and $J =$

diag(J_{ij}) represents the value at each node on Ω^e. The one-dimensional mass matrix is diagonal because of the orthogonal property of the Legendre-Lagrange interpolation polynomials on the GLL nodes, and thus the two-dimensional mass matrix $\mathbf{M}$ is also diagnal. The gradient matrices are defined by

$$\mathbf{D}_1 = e_{\alpha x}\mathbf{D}_x + e_{\alpha y}\mathbf{D}_y,\ \mathbf{D}_2 = \mathbf{D}_x(u_x) + \mathbf{D}_y(u_y),\ \text{and}\ \mathbf{Dq} = \mathbf{D}_x\mathbf{q}_x + \mathbf{D}_y\mathbf{q}_y, \quad (34)$$

where the differentiation matrices can be represented by a tensor product form of the one-diemensional differentiation matrix $\hat{D} = [\hat{D}_{\hat{i}i}] = l'_i(\xi_{\hat{i}})$ as

$$\mathbf{D}_x = \left(\frac{\partial \psi_{ij}}{\partial x}, \psi_{\hat{i}\hat{j}}\right) = G^{\xi x} J[\hat{M} \otimes \hat{M}\hat{D}] + G^{\eta x} J[\hat{M}\hat{D} \otimes \hat{M}], \quad (35)$$

$$\mathbf{D}_y = \left(\frac{\partial \psi_{ij}}{\partial y}, \psi_{\hat{i}\hat{j}}\right) = G^{\xi y} J[\hat{M} \otimes \hat{M}\hat{D}] + G^{\eta y} J[\hat{M}\hat{D} \otimes \hat{M}], \quad (36)$$

where $G^{\xi x} = \text{diag}(G^{\xi x}_{ij})$, $G^{\xi y} = \text{diag}(G^{\xi y}_{ij})$, $G^{\eta x} = \text{diag}(G^{\eta x}_{ij})$, and $G^{\eta y} = \text{diag}(G^{\eta y}_{ij})$ represent the geometric factors $\frac{\partial \xi}{\partial x}$, $\frac{\partial \xi}{\partial y}$, $\frac{\partial \eta}{\partial x}$, and $\frac{\partial \eta}{\partial x}$, respectively, and their values at each node (x_i, y_j). The surface integrations acting on the boundary nodes on each face of the local element in Eqs. (29)–(32) are represented by

$$\mathbf{R}_1\mathbf{f}_\alpha = \sum_{s=1}^{4}\sum_{k=0}^{N} \mathcal{R}^s_k \left\{\mathbf{n} \cdot [\mathbf{F}_\alpha(\bar{f}) - \mathbf{F}^*_\alpha(\bar{f})]\right\} w_k J^s_k, \quad (37)$$

$$\mathbf{R}_2\mathbf{T} = \sum_{s=1}^{4}\sum_{k=0}^{N} \mathcal{R}^s_k \left\{\mathbf{n} \cdot [\mathbf{F}^*(T)_{ij} - \mathbf{F}(T)_{ij}]\right\} w_k J^s_k, \quad (38)$$

$$\mathbf{Rq} = \sum_{s=1}^{4}\sum_{k=0}^{N} \mathcal{R}^s_k \left\{\mathbf{n} \cdot [\mathbf{q}^*_{ij} - \mathbf{q}_{ij}]\right\} w_k J^s_k, \quad (39)$$

$$\mathbf{R}_x\mathbf{T} = \sum_{s=1}^{4}\sum_{k=0}^{N} \mathcal{R}^s_k \{n_x[(T)^*_{ij} - (T)_{ij}]\} w_k J^s_k, \quad (40)$$

$$\mathbf{R}_y\mathbf{T} = \sum_{s=1}^{4}\sum_{k=0}^{N} \mathcal{R}^s_k \{n_y[(T)^*_{ij} - (T)_{ij}]\} w_k J^s_k, \quad (41)$$

where $R^s_k\{\cdot\}$ extracts the information of $\{\cdot\}$ at the nodes situated on each face of the local element for the face number s and J^s_k is the surface Jacobian at the nodes on each face.

The semidiscrete schemes for Eqs. (29)–(30) can be written simply as

$$\frac{d\mathbf{f}_\alpha}{dt} = \mathbf{L}_1\mathbf{f}_\alpha, \tag{42}$$

$$\frac{d\mathbf{T}}{dt} = \mathbf{L}_2\mathbf{T} + \mathbf{D}\mathbf{q} + \mathbf{R}\mathbf{q}, \tag{43}$$

where $\mathbf{L}_1 = \mathbf{M}^{-1}(-\mathbf{D}_1 + \mathbf{R})$ and $\mathbf{L}_2 = \mathbf{M}^{-1}(-\mathbf{D}_2 - \mathbf{R})$. We have shown the matrix structures and eigenvalue distributions for the spatial operator of Eq. (42) in [31]. Figures 1(a) and 1(b) respectively show the matrix structure and eigenvalue distribution for the spatial operator in Eq. (43) with periodic boundary conditions. A uniform spectral element mesh is used with the number of elements $E = 3 \times 3$ and the approximation order $N = 3$. For convenience, we set the velocity $\mathbf{u} = (1, 1)$ and $\chi = 1$. The eigenvalue distributions reside all on the negative half-plane so that we can choose the fourth-order, five-stage Runge-Kutta (RK) time integration method [37] with the stability region slightly larger and with less memory than those of the classical RK methods.

4. Computational Results

In this section, we show computational results and validation for two benchmark problems on natural convection flows in a square cavity and a horizontal concentric annulus in two dimensions.

4.1. Parameter Setting for Benchmark Studies

For natural convection flows, we consider a Bousinessq approximation [9] with the forcing term $\mathbf{G}$ in Eqs. (1) and (11) defined as

$$\mathbf{G} = \rho\mathbf{g}\beta(T - T_o), \tag{44}$$

where $T_o = (T_h + T_c)/2$ is the average of the two different temperatures ($T_h > T_c$), $\mathbf{g}$ is the gravitational acceleration, and β is the thermal expansion coefficient, which is constant in space and time in the framework of the Bousinessq approximation.

We characterize natural convection flows with two nondimensional numbers, the Rayleigh number (Ra) and the Prandtl number (Pr). Both are defined in the following way

$$Ra = \frac{\beta|\mathbf{g}|(T_h - T_c)L^3}{\nu\chi} \quad \text{and} \quad Pr = \frac{\nu}{\chi}, \tag{45}$$

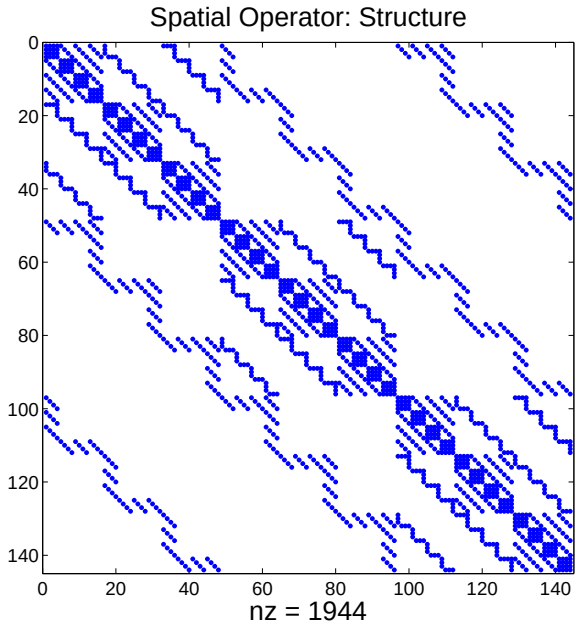

(a) Spatial Operator

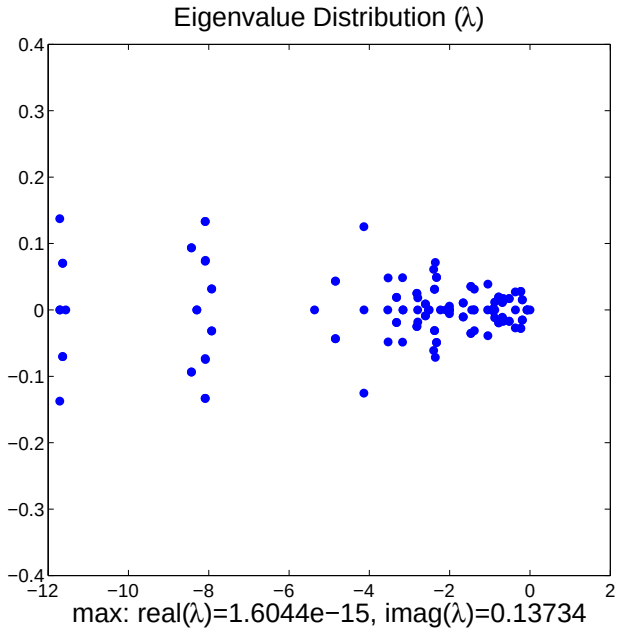

(b) Eigenvalue spectrum

Figure 1: Spatial Operator and Eigenvalue Spectrum for Eq. (43) for $E = 9$ and $N = 3$ with periodic boundary conditions

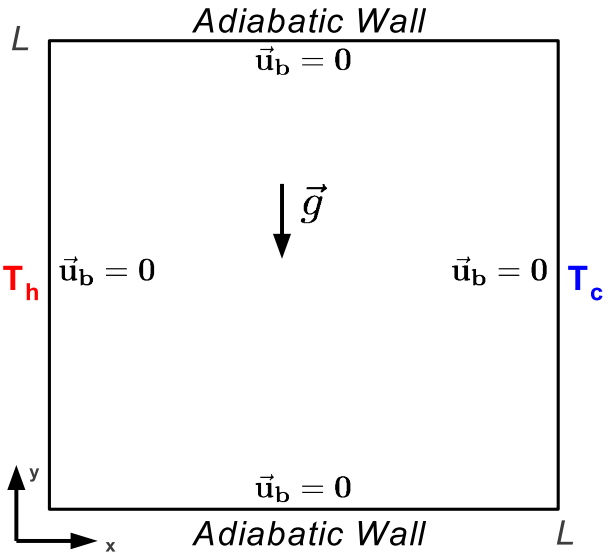

Figure 2: Geometry and boundary conditions of natural convection in a square cavity.

where L is a characteristic length of the computational domain. As mentioned above, χ is the thermal diffusivity, and ν is the kinematic viscosity. We define the characteristic velocity

$$U^* = \sqrt{\frac{Ra}{Pr}}\frac{\nu}{L}. \tag{46}$$

We ensure our characteristic velocity is in the low Mach number regime, typically $Ma = 0.01$, so that

$$U^* \leq c_s Ma. \tag{47}$$

The dimensionless relaxation time τ is determined through the relation $\nu = \tau c_s^2 \delta t$ where we determine the time-step size δt from $CFL = \frac{\max_\alpha |\mathbf{e}_\alpha| \delta t}{\Delta \mathbf{x}_{\min}} = 0.1$, where $\Delta \mathbf{x}_{\min}$ is the minimum grid spacing in our mesh.

4.2. Natural Convection in a Square Cavity

We performed steady-state natural convection flow simulations in a square cavity. The geometry is shown in Figure 2. The initial velocity is set as

$\mathbf{u} \equiv (0,0)$ and the initial density $\rho \equiv 1$. The wall boundary conditions for the velocity fields are given as $\mathbf{u}_b = (0,0)$ and the nonhomogeneous Dirichlet boundary conditions for the temperature as $T(0,y,t) = T_h$ and $T(L,y,t) = T_c$. The adiabatic boundary conditions are set as $\frac{\partial T}{\partial y}|_{(x,0,t)} = \frac{\partial T}{\partial y}|_{(x,L,t)} = 0$.

Table 1: Convergence of Nu_o, Nu_o^{max}, and Nu_o^{min} for $Ra = 10^3$

SEDG-LBM (N)	Nu_o	Nu_o^{max}	Nu_o^{min}
3	1.1165	1.5261	0.6847
5	1.1177	1.5063	0.6916
7	1.1178	1.5063	0.6913
9	1.1178	1.5063	0.6913
Wang *et al.* [39]	1.1178	1.5063	0.6912
De Vahl Davis [41]	1.117	1.505	0.692

Table 2: Convergence of Nu_o, Nu_o^{max}, and Nu_o^{min} for $Ra = 10^4$

SEDG-LBM (N)	Nu_o	Nu_o^{max}	Nu_o^{min}
3	2.2236	3.7078	0.5413
5	2.2447	3.5303	0.5863
7	2.2448	3.5306	0.5852
9	2.2448	3.5309	0.5851
Wang *et al.* [39]	2.2448	3.5310	0.5849
Hortmann *et al.* [40]	2.24475	3.53087	-
De Vahl Davis [41]	2.238	3.528	0.586

Figure 3 shows the streamlines and isotherms of the square cavity flows at $Ra = 10^3, 10^4, 10^5$. The effect of Ra is evident in these figures. In particular, a given isotherm is passively advected throughout the domain to greater degree as Ra increases.

Simulations are performed on a uniform spectral element mesh with $E = 256$ and a fixed polynomial order of $N = 5$, involving the total number of grids $\mathcal{N} = (N+1)^2 E$. Figure 4 demonstrates good convergence of the temperature profiles with increasing polynomial order N on the same mesh. The profiles are shown at the horizontal line $y = 0.5$ and at the vertical line $x = 0.5$.

We also show the convergence of the Nusselt number Nu_o along the axis $x = 0$, where the Dirichlet boundary condition $T = T_h$ is specified. We

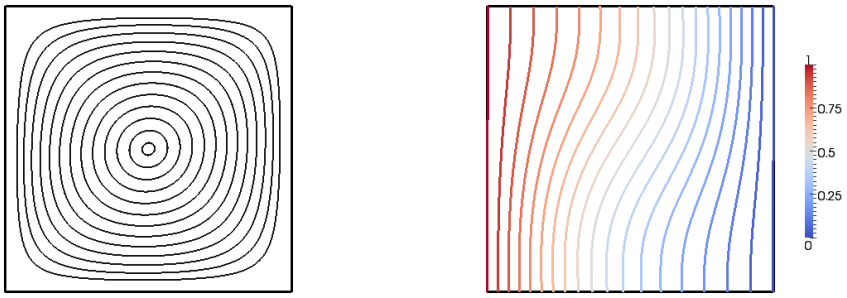

(a) $Ra = 10^3$, $Pr = 0.7$

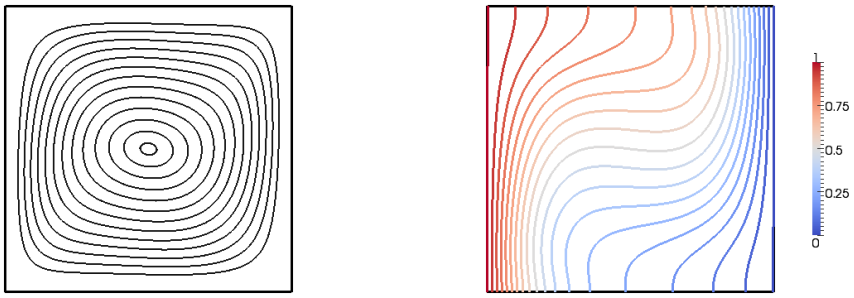

(b) $Ra = 10^4$, $Pr = 0.7$

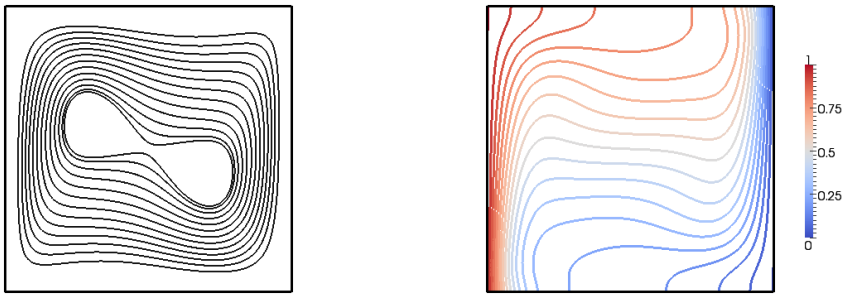

(c) $Ra = 10^5$, $Pr = 0.7$

Figure 3: Streamlines (left) and isotherms (right) of natural convection cavity flow; $E = 256$ and $N = 5$.

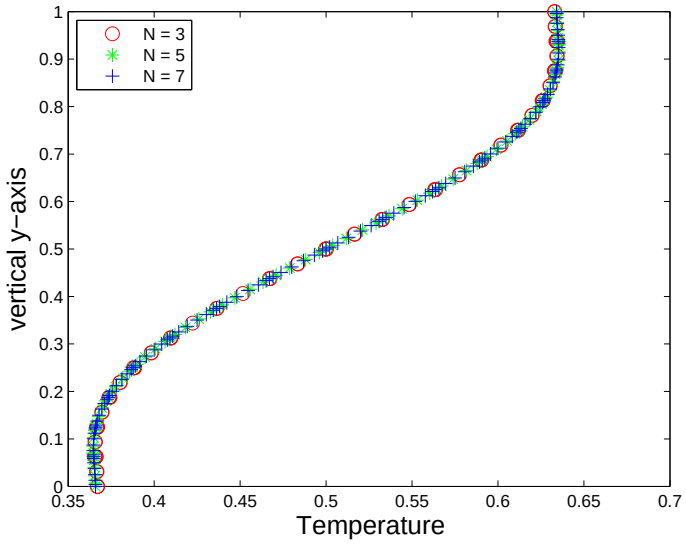

(a) Temperature Profile at $x = 0.5$

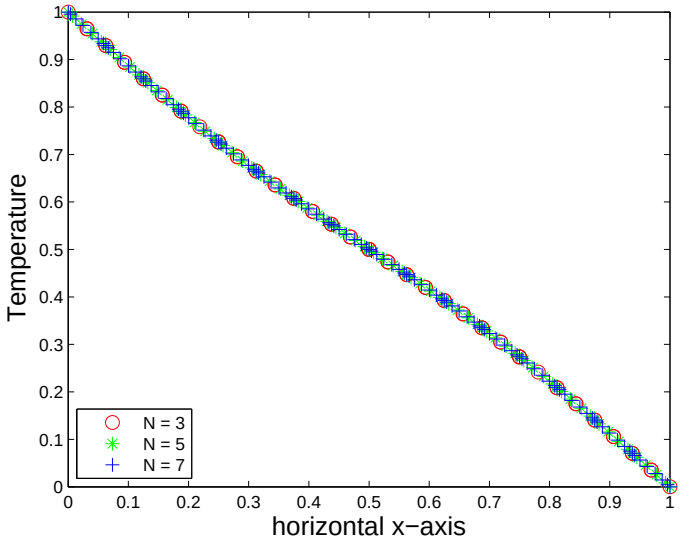

(b) Temperature Profile at $y = 0.5$

Figure 4: Temperature profiles for natural convection square cavity flow at $Ra = 1000$, demonstrating convergence of the solution for increasing $N = 3, 5, 7$ with $E = 256$.

Table 3: Convergence of Nu_o, Nu_o^{max}, and Nu_o^{min} for $Ra = 10^5$

SEDG-LBM (N)	Nu_o	Nu_o^{max}	Nu_o^{min}
3	4.3187	9.5203	0.3362
5	4.5191	7.6878	0.7310
7	4.5216	7.7184	0.7295
9	4.5216	7.7189	0.7286
Wang *et al.* [39]	4.5214	7.7161	0.7279
Hortmann *et al.* [40]	4.52164	7.72013	-
De Vahl Davis [41]	4.509	7.717	0.729

compute the Nusselt number defined by

$$Nu_o = \int_0^1 q_x|_{x=0} dy, \tag{48}$$

where

$$q_x = u_x T - \frac{\partial T}{\partial x}. \tag{49}$$

In Tables 1–3, we demonstrate the convergence studies of the Nusselt number for varying polynomial order $N = 3, 5, 7, 9$, including local minimum and maximum values, with validation to those by Wang *et al.* [39], Hortmann *et al.* [40] and De Vahl Davis. [41]. Our results show good agreement compared with the results of others.

4.3. Natural Convection in a Horizontal Concentric Annulus

We studied steady-state natural convection flows inside a horizontal concentric annulus. The geometry and boundary conditions of the problem are provided in Figure 5.

We set the initial velocity $\mathbf{u} \equiv (\mathbf{0}, \mathbf{0})$ and the initial density $\rho \equiv 1$. Wall boundary conditions for the velocity field are $\mathbf{u}_b = (0, 0)$, and temperature boundary conditions are given as $T(r = r_i, \varphi, t) = T_h = 1$ and $T(r = r_o, \varphi, t) = T_c = 0$. We use the radius ratio $\frac{r_o}{r_i} = 2.6$ and the characteristic length $L = r_o - r_i$.

Figure 6 shows the streamlines and isotherms of the horizontal annulus cavity flows at $Ra = 10^3, 10^4, 5 \times 10^4$ on a spectral element mesh (see Figure 7(a)) with $E = 512$ and $N = 5$. Again, the effect of Ra is evident. In particular, a given isotherm is passively advected throughout the domain to greater degree as Ra increases.

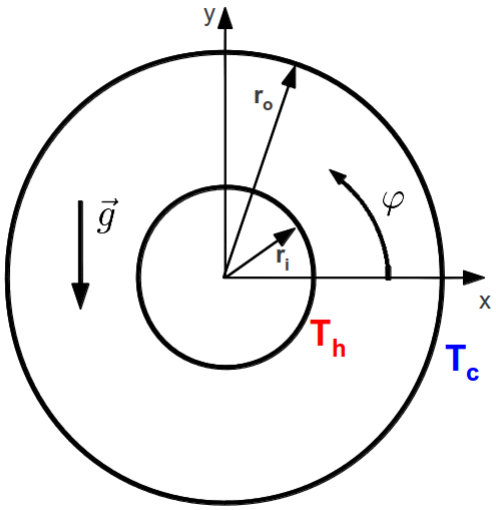

Figure 5: Geometry and boundary conditions of natural convection in a horizontal concentric annulus.

We also compute the average Nusselt number Nu_{avg} defined by

$$Nu_{avg} = \frac{1}{2}(Nu_{inner} + Nu_{outer}), \tag{50}$$

where

$$Nu_{inner} = -\frac{1}{\pi}\int_{-\frac{\pi}{2}}^{\frac{\pi}{2}} r_i \frac{\partial T}{\partial r}|_{r=r_i} d\varphi, \tag{51}$$

$$Nu_{outer} = -\frac{1}{\pi}\int_{-\frac{\pi}{2}}^{\frac{\pi}{2}} r_o \frac{\partial T}{\partial r}|_{r=r_o} d\varphi. \tag{52}$$

Tables 4–6 show convergence of the average Nusselt number Nu_{avg} on Mesh A as increasing $N = 3, 5, 7, 9$. We compare our results with those by Kuehn and Goldstein [42], who solve the Navier-Stokes equations by a finite-difference method. When compared with the results by Kuehn and Goldstein, our results are within 5% accuracy.

We examined details of the difference between our SEDG-LBM results and those from [42] in the temperature profiles at $\varphi = -\frac{\pi}{2}, 0, \frac{\pi}{2}$, demonstrating the comparison in Figure 8. We observe that the SEDG-LBM results

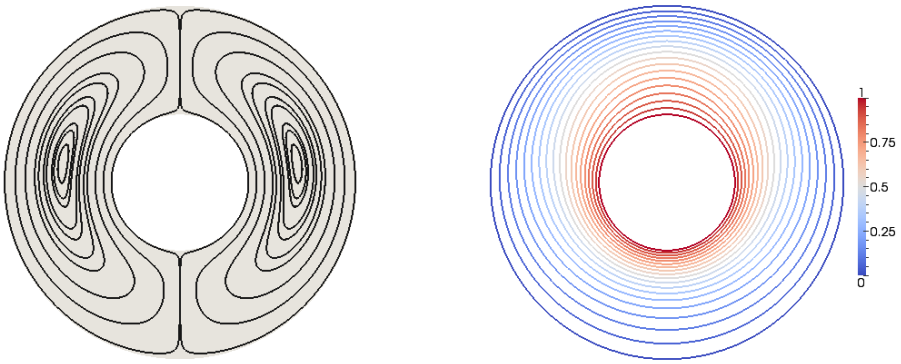

(a) $Ra = 10^3$, $Pr = 0.7$

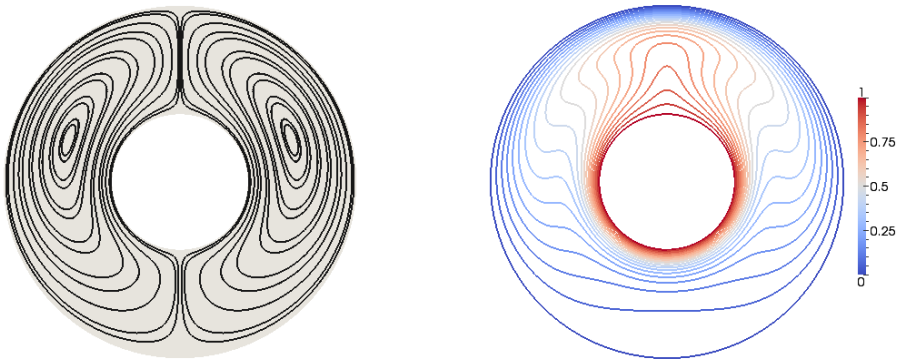

(b) $Ra = 10^4$, $Pr = 0.7$

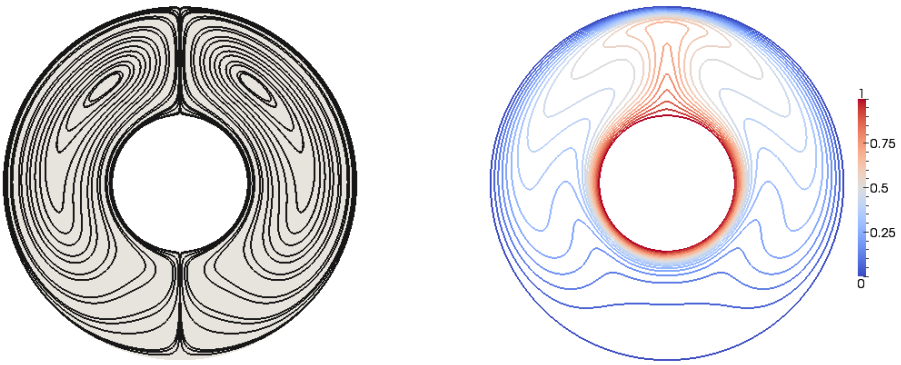

(c) $Ra = 5 \times 10^4$, $Pr = 0.7$

Figure 6: Streamlines (left) and isotherms (right) of natural convection in a horizontal annulus, using $N = 5$ on Mesh A.

agree well with those by Kuehn and Goldstein for $\varphi = 0$. However, we observe some discrepancy in the range of $r^* = 0.1 \sim 0.3$ and $r^* = 0.2 \sim 0.9$ for the cases of $\varphi = -\frac{\pi}{2}$ and $\varphi = \frac{\pi}{2}$, respectively, as shown in Figure 8. These explain the discrepancy in the comparison of Nu_{avg} in Tables 4–6.

Given this difference in Nu_{avg} and temperature profile, we further seek to verify our results against another benchmark. For this study, we simulate natural convection within a horizontal concentric annulus using Nek5000 [38], the open-source Navier-Stokes solver based on the spectral element method. Using Nek5000 on Mesh A with a high polynomial approximation, $N = 11$, we determine temperature profiles and average Nusselt numbers and use this data as new benchmarks. Our SEDG-LBM simulations are performed on Mesh B (see Figure 7(b)) with $E = 256$. Figure 9 demonstrates the convergence of temperature profiles for our SEDG-LBM results $\varphi = -\frac{\pi}{2}, 0, \frac{\pi}{2}$ for $Ra = 5 \times 10^4$ and $Pr = 0.7$, showing good agreement with those of Nek5000.

In Tables 7–9, we show the convergence of Nu_{avg} with $N = 3, 5, 7, 9$ by the SEDG-LBM on Mesh B for $Ra = 10^3, 10^4, 5 \times 10^4$. Our results agree well with those by Nek5000 simulations with $N = 11$. These tables show the advantage of the SEDG approximation. In particular, SEDG-LBM results on the non-uniform coarse mesh (i.e. Mesh B) which exhibit better resolution in the boundary layer region is able to achieve the same accuracy as the SEDG-LBM results determined on the refined mesh (i.e. Mesh A) as given in Tables 4, 5, and 6.

Table 4: Convergence of Nu_{avg} for $Ra = 10^3$

SEDG-LBM (N) on Mesh A	Nu_{avg}
3	1.1295
5	1.1325
7	1.1325
9	1.1325
Kuehn and Goldstein [42]	1.083

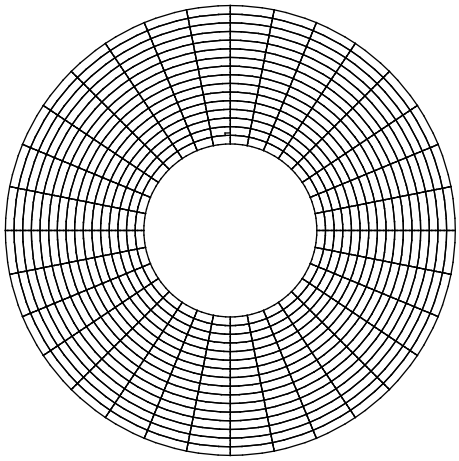

(a) Mesh A with $E = 512$

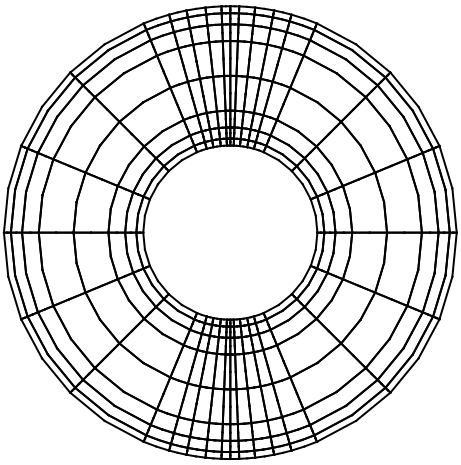

(b) Mesh B with $E = 256$

Figure 7: Two different meshes used for the horizontal annulus simulations

Table 5: Convergence of Nu_{avg} for $Ra = 10^4$

SEDG-LBM (N) on Mesh A	Nu_{avg}
3	2.0615
5	2.0704
7	2.0705
9	2.0705
Kuehn and Goldstein [42]	2.008

Table 6: Convergence of Nu_{avg} for $Ra = 5 \times 10^4$

SEDG-LBM (N) on Mesh A	Nu_{avg}
3	3.0309
5	3.0950
7	3.0956
9	3.0956
Kuehn and Goldstein [42]	2.999

Table 7: Convergence of Nu_{avg} for $Ra = 10^3$

SEDG-LBM (N) on Mesh B	Nu_{avg}
3	1.2034
5	1.1310
7	1.1325
9	1.1325
Nek5000 ($N = 11$)	1.1325

Table 8: Convergence of Nu_{avg} for $Ra = 10^4$

SEDG-LBM (N) on Mesh B	Nu_{avg}
3	2.2195
5	2.0774
7	2.0702
9	2.0705
Nek5000 ($N = 11$)	2.0705

Table 9: Convergence of Nu_{avg} for $Ra = 5 \times 10^4$

SEDG-LBM (N) on Mesh B	Nu_{avg}
3	3.0218
5	3.1055
7	3.0975
9	3.0958
Nek5000 ($N = 11$)	3.0956

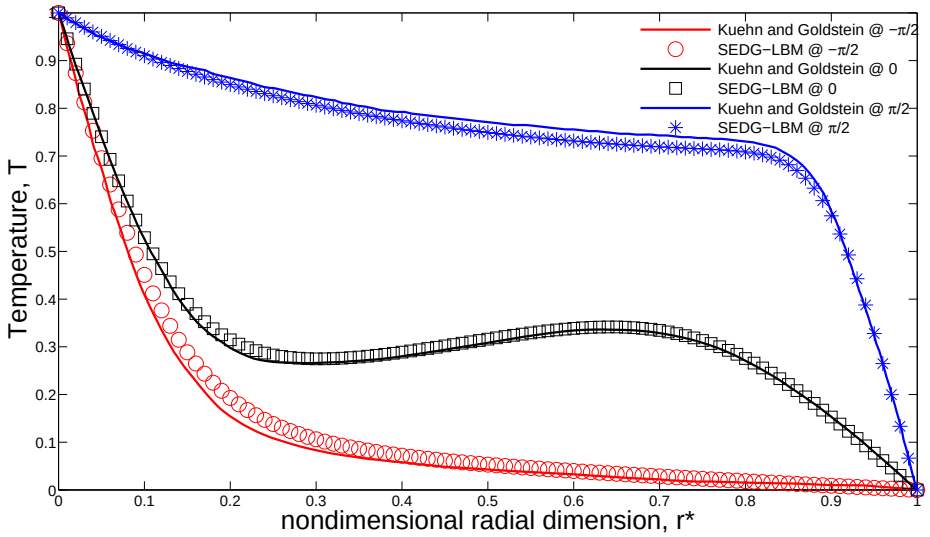

Figure 8: Temperature profiles of SEDG-LBM results vs. Reference [42] for horizontal annulus simulation at $Ra = 5 \times 10^4$ and $Pr = 0.7$ for $\varphi = \frac{\pi}{2}$, $\varphi = 0$, and $\varphi = -\frac{\pi}{2}$. Polynomial order for SEDG-LBM is $N = 9$. The nondimensional radius, r^* is defined as $r^* = \frac{r - r_i}{L}$. SEDG-LBM computations were performed on Mesh (A).

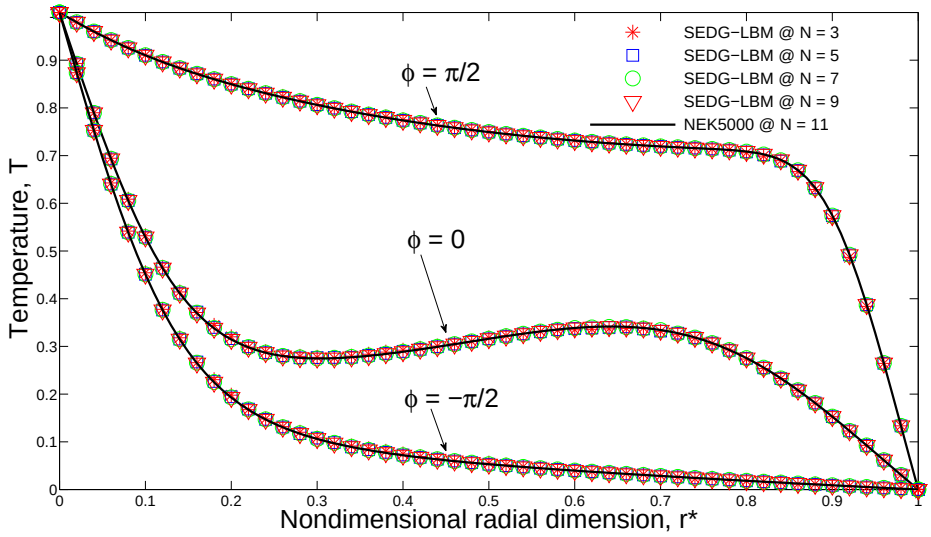

Figure 9: Temperature profile of SEDG-LBM results vs. Nek5000 [38] for horizontal annulus simulation at $Ra = 5 \times 10^4$ and $Pr = 0.7$ for $\varphi = \frac{\pi}{2}$, $\varphi = 0$, and $\varphi = -\frac{\pi}{2}$. Polynomial orders for SEDG-LBM are $N = 3, 5, 7$ and 9. Polynomial order for Nek5000 is $N = 11$. Both SEDG-LBM and Nek5000 computations were performed on Mesh (B).

5. Conclusions

We have presented a spectral-element discontinuous Galerkin lattice Boltzmann method for solving two-dimensional incompressible natural convection flows. In particular, we have presented results for natural convection in a square cavity and a horizontal concentric annulus. Our formulation extends the work done by Min and Lee [31] to incorporate into the discrete Boltzmann and lattice Boltzmann equations a forcing term that is in accordance with the Bousinessq approximation. We resolved the temperature field by applying an SEDG discretization in space to the advection-diffusion equation and apply boundary conditions weakly through a proper treatment of the numerical flux based on the Lax-Friedrichs and central Fluxes. We used a passive-scalar approach that allows us to investigate flows for variable Prandtl number and to compute the temperature field cost-effectively by solving only one equation, rather than solving multiple equations such as in the double-distribution approach. We have examined square cavity flows for $Ra = 10^3 \sim 10^5$ and flows in a horizontal concentric annulus for $Ra = 10^3 \sim 5 \times 10^4$, provided with convergence studies in the temperature

profiles and Nusselt numbers. Computational results show good agreement with those by a finite-difference method, a finite-volume method, a multiple-relaxation-time LBM, and a spectral element method [38].

Extension to three dimensions and performance studies in comparison to other approaches, such as double-distribution thermal lattice Boltzmann methods, remain as future work.

Acknowledgments

This work is supported in part from the DOE, Office of Nuclear Energy's Nuclear Energy University Programs and in part from the U.S. Department of Energy, under Contract DE-ACO2-O6CH11357. We thank Alexsandr Obabko for his help and guidance in the proper execution of the Nek5000 code.

[1] F.J. Alexander, S. Chen, J.D. Sterling, Lattice Boltzmann thermohydrodynamics, *Phys. Rev. E* **47** 4 (1993) R2249.

[2] Y. Chen, H. Ohashi, M. Akiyama, Thermal lattice Bhatnagar-Gross-Krook model without nonlinear deviations in macrodynamic equations, *Phys. Rev. E* **50** 4 (1994) 2776-2783.

[3] X. Shan, H. Chen, Lattice Boltzmann model for simulating flows with multiple phases and components, *Phys. Rev. E* **47** 3 (1993) 1815-1819.

[4] G.R. McNamara, A.L. Garcia, B.J. Alder, Stabilization of thermal lattice Boltzmann models, *J. Stat. Phys.* **81** (1995) 1/2 395-408.

[5] G. Vahala, P. Pavlo, L. Vahala, N.S. Martys, Thermal lattice-Boltzmann models (TLBM) for compressible flows, *Int. J. Mod. Phys. C* **9** 8 (1998) 1247-1261.

[6] N.I. Prasianakis, I.V. Karlin, Lattice Boltzmann method for thermal flow simulation on standard lattices, *Phys. Rev. E* **76** (2007) 016702.

[7] M. Watari, M. Tsutahara, Two-dimensional thermal model of the finite-difference lattice Boltzmann method with high spatial isotropy, *Phys. Rev. E* **67** (2003) 036306.

[8] M. Soe, G. Vahala, P. Pavlo, L. Vahala, H. Chen, Thermal lattice Boltzmann simulations of variable Prandtl number turbulent flows, *Phys. Rev. E* **57** 4 (1998) 4227-4237.

[9] X. Shan, Simulation of Rayleigh-Bénard convection using a lattice Boltzmann method, *Phys. Rev. E* **55** 3 (1997) 2780-2788.

[10] X. He, S. Chen, G.D. Doolen, A novel thermal model for the lattice Boltzmann method in incompressible limit, *J. Comput. Phys.* **146** 1 (1998) 282-300.

[11] B. Palmer, D. Rector, Lattice Boltzmann algorithm for simulating thermal flow in compressible fluids, *J. Comput. Phys.* **161** 1 (2000) 1-20.

[12] Y. Peng, C. Shu, Y.T. Chew, Simplified thermal lattice Boltzmann model for incompressible thermal flows, *Phys. Rev. E* **68** (2003) 026701.

[13] Y. Shi, T.S. Zhao, Z.L. Guo, Thermal lattice Bhatnagar-Gross-Krook model for flows with viscous heat dissipation in the incompressible limit, *Phys. Rev. E* **70** (2004) 066310.

[14] Z. Guo, C. Zheng, B. Shi, T.S. Zhao, Thermal lattice Boltzmann equation for low Mach number flows: Decoupling model, *Phys. Rev. E* **75** (2007) 036704.

[15] C.S. Nor Azwadi, T. Tanahashi, Simplified thermal lattice Boltzmann in incompressible limit, *Int. J. Mod. Phys. B* **20** 17 (2006) 2437-2449.

[16] H.N. Dixit, V. Babu, Simulation of high Rayleigh number natural convection in a square cavity using the lattice Boltzmann method, *Int. J. Heat and Mass Trans.* **49** 3 (2006) 727-739.

[17] X. He, L.S. Luo, M. Dembo, Some progress in lattice Boltzmann method. Part 1. Nonuniform mesh grids, *J. Comput. Phys.* **129** (1996) 357-363.

[18] Y. Shi, T.S. Zhao, Z.L. Guo, Finite difference-based lattice Boltzmann simulation of natural convection heat transfer in a horizontal concentric annulus, *Comp. Fluids* **35** 1 (2006) 1-15.

[19] Z. Guo, T.S. Zhao, Explicit finite-difference lattice Boltzmann method for curvilinear coordinates, *Phys. Rev. E* **67** (2003) 066709.

[20] C. Shu, Y. Peng, Y.T. Chew, Simulation of natural convection in a square cavity by Taylor series expansion- and least squares-based lattice Boltzmann method, *Int. J. Mod. Phys. C* **13** 10 (2002) 1399-1414.

[21] Y. Peng, Y.T. Chew, C. Shu, Numerical simulation of natural convection in a concentric annulus between a square outer cylinder and a circular inner cylinder using the Taylor-series-expansion and least-squares-based lattice Boltzmann method, *Phys. Rev. E* **67** (2003) 026701.

[22] S. Succi, G. Amati, R. Benzi, Challenges in lattice Boltzmann computing, *J. Stat. Phys.* **81** (1995) 5-16.

[23] P. Lallemand, L-S. Luo, Theory of the lattice Boltzmann method: Acoustic and thermal properties in two and three dimensions, *Phys. Rev. E* **68** (2003) 036706.

[24] Q. Zou, X. He, On pressure and velocity boundary conditions for the lattice boltzmann BGK model, *Phys. Fluids* **9** 6 (1997) 1591-1598.

[25] O. Filippova, D. Hänel, Grid refinement for lattice-BGK models, *J. Comput. Phys.* **147** 1 (1998) 219-228.

[26] R. Mei, L-S. Luo, W. Shyy, An accurate curved boundary treatment in the lattice Boltzmann method, *J. Comput. Phys.* **229** 2 (1999) 307-330.

[27] P. Lallemand, L-S. Luo, Lattice Boltzmann method for moving boundaries, *J. Comput. Phys.* **184** 2 (2003) 406-421.

[28] A.D'Orazio, M. Corcione, G.P. Celata, Application to natural convection enclosed flows of a lattice Boltzmann BGK model coupled with a general purpose thermal boundary condition, *Int. J. Heat and Mass Trans.* **43**6 (2004) 575-586.

[29] G.H. Tang, W.Q. Tao, Y.L. He, Thermal boundary condition for the thermal lattice Boltzmann equation, *Phys. Rev. E* **72** (2005) 016703.

[30] C-H. Liu, K-H. Lin, H-C. Mai, C-A. Lin, Thermal boundary conditions for thermal lattice Boltzmann simulations, *Comp. Math. Appl.* **59** 7 (2010) 2178-2193.

[31] M. Min, T. Lee, A spectral-element discontinuous Galerkin lattice Boltzmann method for nearly incompressible flows, *J. Comput. Phys.* **230** 1 (2011) 245-259.

[32] X. He, X. Shan, G.D. Doolen, Discrete Boltzmann equation model for nonideal gases, *Phys. Rev. E* **57** 1 (1998) R13.

[33] Y.H. Qian, D. D'Humières, P. Lallemand, Lattice BGK models for Navier-Stokes equation, *Europhys. Lett.* **17** (1992) 479-484.

[34] T. Lee, C.-L. Lin, An Eulerian description of the streaming process in the lattice Boltzmann equation, *J. Comput. Phys.* **185** 2 (2003) 445-471.

[35] J.S. Hesthaven and T. Warburton, Nodal discontinuous Galerkin methods, algorithms, analysis, and applications, *Texts in Applied Mathematics* (Springer, 2008).

[36] M.O. Deville, P.F. Fischer, E.H. Mund, High-order methods for incompressible fluid flow, *Cambridge Monographs on Applied and Computational Mathematics* (Cambridge University Press, 2002).

[37] M.H. Carpenter, C. Kennedy, Fourth-order $2N$-storage Runge-Kutta schemes, NASA Report TM 109112, NASA Langley Research Center (1994).

[38] P. Fischer, J. Lottes, D. Pointer, A. Siegel, Petascale algorithms for reactor hydrodynamics, *Journal of Physics: Conference Series* **125** 1 (2008) 012076.

[39] J. Wang, D. Wang, P. Lallemand, L. Luo, Lattice Boltzmann simulations of thermal convective flows in two dimensions, *Comp. Math. Appl.* **65** 2 (2013) 262-286.

[40] M. Hortmann, M. Perić, G. Scheuerer, Finite volume multigrid prediction of laminar natural convection: Bench-mark solutions, *Int. J. Numer. Meth. Fluids* **11** 2 (1990) 189-207.

[41] G. De Vahl Davis, Natural convection of air in a square cavity: A benchmark numerical solution, *Int. J. Numer. Meth. Fluids* **3** 3 (1983) 249-264.

[42] T.H. Kuehn, R.J. Goldstein, An experimental and theoretical study of natural convection in the annulus between horizontal concentric cylinders, *J. Fluid Mech.* **74** 4 (1976) 695-719.